

Abundance matching with the mean star formation rate: there is no missing satellites problem in the Milky Way above $M_{200} \sim 10^9 M_{\odot}$

J. I. Read^{1*}, D. Erkal¹

¹*Department of Physics, University of Surrey, Guildford, GU2 7XH, UK*

13 May 2019

ABSTRACT

We introduce a novel abundance matching technique that produces a more accurate estimate of the pre-infall halo mass, M_{200} , for satellite galaxies. To achieve this, we abundance match with the mean star formation rate, averaged over the time when a galaxy was forming stars, $\langle \text{SFR} \rangle$, instead of the stellar mass, M_* . Using data from the Sloan Digital Sky Survey, the GAMA survey and the Bolshoi simulation, we obtain a statistical $\langle \text{SFR} \rangle - M_{200}$ relation in Λ CDM. We then compare the pre-infall halo mass, M_{200}^{abund} , derived from this relation with the pre-infall dynamical mass, M_{200}^{dyn} , for 21 nearby dSph and dIrr galaxies, finding a good agreement between the two. As a first application, we use our new $\langle \text{SFR} \rangle - M_{200}$ relation to empirically measure the cumulative mass function of a volume-complete sample of bright Milky Way satellites within 280 kpc of the Galactic centre. Comparing this with a suite of cosmological ‘zoom’ simulations of Milky Way-mass halos that account for subhalo depletion by the Milky Way disc, we find no missing satellites problem above $M_{200} \sim 10^9 M_{\odot}$ in the Milky Way. We discuss how this empirical method can be applied to a larger sample of nearby spiral galaxies.

Key words: cosmology: dark matter; cosmology: observations; galaxies: abundances; galaxies: dwarf; galaxies: haloes; galaxies: kinematics and dynamics.

1 INTRODUCTION

The standard Λ CDM cosmological model makes concrete predictions for the growth of dark matter structure over cosmic time (e.g. White & Rees 1978; Frenk et al. 1988). This produces an excellent description of the distribution of mass in the Universe on large scales ($\gtrsim 10$ Mpc) (e.g. Springel et al. 2006; Percival 2013). However, on smaller scales there have been long-standing tensions. Key amongst these is the “missing satellites problem” (Moore et al. 1999; Klypin et al. 1999). Pure dark matter structure formation simulations predict many more bound dark matter halos than visible satellites around the Milky Way and M31 (and see e.g. Bullock & Boylan-Kolchin 2017, for a review). Despite the recent explosion in the numbers of dwarf galaxies found by large surveys (e.g. Belokurov et al. 2007; Ibata et al. 2007; McConnachie 2012; Bechtol et al. 2015; Drlica-Wagner et al. 2015; Koposov et al. 2015), this problem still persists today (e.g. Koposov et al. 2008; Tollerud et al. 2008).

Reasonable assumptions about galaxy formation can be

made that will solve the missing satellites problem, typically by assuming that some subhalos light up with stars while others remain dark (e.g. Macciò et al. 2010; Sawala et al. 2016). However, even the latest galaxy formation simulations find very different results at the scale of dwarf galaxies (e.g. Mayer et al. 2008; Scannapieco et al. 2012; Contenta et al. 2017). As a result, many proposed solutions to the missing satellites problem disagree in the details. Some are unable to simultaneously produce the mass function and radial distribution of the satellites (e.g. Koposov et al. 2008), or their internal kinematics (e.g. Read et al. 2006b; Boylan-Kolchin et al. 2011); some are even mutually exclusive, relying on the formation of dark matter cores due to bursty stellar feedback (e.g. Zolotov et al. 2012; Wetzel et al. 2016), or not requiring this at all (e.g. Sawala et al. 2016; Fattahi et al. 2016).

Each of the above solutions places the Milky Way satellites in different pre-infall dark matter halos. Thus, an empirical method for mapping visible galaxies to dark matter halos would allow us to determine which, if any, of the above models is correct. This is the goal of ‘abundance matching’. In its simplest form, abundance matching statistically

* E-mail: justin.inglis.read@gmail.com

maps galaxies of an observed number density in the Universe to dark matter halos of the same number density selected from a cosmological N -body simulation (e.g. Peacock & Smith 2000; Kravtsov et al. 2004; Vale & Ostriker 2004, 2006). From this mapping, we can then derive a statistical relationship between some galaxy property, \mathcal{G} , and its dark matter halo mass, M_{200} . Although \mathcal{G} is usually taken to be the stellar mass of a galaxy, M_* , abundance matching can be used to link *any* galaxy property to halo mass, so long as the property in question rises monotonically with M_{200} , and has negligible scatter.

Once a statistical relationship between \mathcal{G} and M_{200} has been established, we can compare this with direct measurements of \mathcal{G} and M_{200} to probe cosmological models and test galaxy formation theories. This has the advantage that, while \mathcal{G} must be measured for a large sample of galaxies that have a known selection function, the dark matter halo mass M_{200} – which is typically harder to estimate – need only be inferred for a subset of galaxies with excellent quality data. To date, this sort of comparison has only been performed using stellar masses ($\mathcal{G} \equiv M_*$) obtained from Spectral Energy Distribution (SED) model fitting (e.g. Wuyts et al. 2009; Walcher et al. 2011; Mitchell et al. 2013) and M_{200} obtained from either gravitational lensing, or HI rotation curves (e.g. Mandelbaum et al. 2006; Moster et al. 2010; Kravtsov et al. 2014; Read et al. 2017; Katz et al. 2017). These studies find that Λ CDM gives a good representation of the data over an impressive mass range of $5 \times 10^9 \lesssim M_{200}/M_\odot \lesssim 10^{15}$.

While M_* has been used successfully for abundance matching of isolated ‘central’ galaxies, for satellites it is more problematic. Satellites have their star formation shut down (‘quenched’) on infall to a larger galaxy or group (e.g. Peng et al. 2012; Geha et al. 2012; Gatto et al. 2013). This ‘freezes-in’ their stellar mass, causing them to scatter below the $M_* - M_{200}$ relation for isolated dwarfs (e.g. Ural et al. 2015; Contreras et al. 2015; Read et al. 2017). Satellites also experience mass loss due to tidal stripping and shocking, causing them to scatter above relation (e.g. Read et al. 2006a; Tozoeu et al. 2016; and see Figure 3). One solution to these problems is to model this scatter statistically as a ‘nuisance’ parameter (e.g. Reddick et al. 2013; Garrison-Kimmel et al. 2017a; Jethwa et al. 2018). However, this limits our ability to probe cosmological models or test galaxy formation theories. An alternative approach is to directly match satellites to subhalos in numerical simulations (e.g. Madau et al. 2008; Boylan-Kolchin et al. 2012; Brook et al. 2014; Kim et al. 2017). However, again there is some freedom in how to do this (e.g. selecting the halos which are the most massive before infall, the most massive before some redshift, or selecting them stochastically, e.g. Diemand et al. 2007; Reddick et al. 2013). Finally, ‘semi-analytic’ galaxy formation models explicitly model the effect of tides and quenching for satellites in a given cosmology (e.g. Zentner et al. 2005; Baugh 2006). As with the other approaches above, this removes the key advantage of classical abundance matching that it is entirely empirical.

In this paper, we present a new abundance matching method that is designed to work equally well for central galaxies and satellites, while retaining a purely empirical mapping between galaxies and their (sub-)halos. The key idea is to abundance match with the *mean star formation rate*, $\langle \text{SFR} \rangle$, of galaxies (averaged over the time during which

the galaxy was forming stars) instead of the stellar mass. It has already been shown that, for isolated galaxies, the stellar mass is monotonically related to the halo mass (e.g. Moster et al. 2010; Kravtsov et al. 2014; Read et al. 2017; Katz et al. 2017). Thus, the $\langle \text{SFR} \rangle$ of isolated galaxies, as defined above, must also monotonically rise with M_{200} . However, as we shall show in this paper, the advantage of using the $\langle \text{SFR} \rangle$ over M_* is that, for satellite galaxies, it has less scatter at a given pre-infall M_{200} , increasing the accuracy of the abundance matching mass estimator, M_{200}^{abund} .

Our new abundance matching method alleviates the problem of scatter in M_* due to satellite quenching, but does not solve the problem of scatter due to tidal mass loss. We argue, however, that this is only a problem if a satellite loses significant *stellar mass*. If a satellite loses its outer dark matter halo, its stellar mass will be unchanged. As such, its abundance matching mass, M_{200}^{abund} – that is a statistical estimate of the *pre-infall* halo mass of the satellite, M_{200} , derived from the stellar mass and an estimate of the integrated star formation time (see §4.1) – will also be unchanged. Tidal mass loss can, however, still present a problem for our *dynamical* estimates of the pre-infall halo mass, M_{200}^{dyn} . We will need M_{200}^{dyn} for at least some satellites to validate our M_{200}^{abund} estimator (see §5.1). Like M_{200}^{abund} , however, tidal mass loss will only become a problem for our estimates of M_{200}^{dyn} if the satellite loses mass down to radii approaching its half light radius (e.g. Read et al. 2006b; Er-rani et al. 2018; Read et al. 2018). Even in this ‘strong tides’ case, we can correct for stellar mass loss if the stellar tidal tails are visible (e.g. Niederste-Ostholt et al. 2010, 2012), while the dynamics of stars in the tidal tails can also be used to determine M_{200}^{dyn} (e.g. Gibbons et al. 2017).

The goal of this paper is to quantitatively explore our novel abundance matching with the $\langle \text{SFR} \rangle$, with an initial application to a volume-complete sample of bright satellite galaxies within 280 kpc of the centre of the Milky Way. Comparing the cumulative mass function of these, determined from the $\langle \text{SFR} \rangle - M_{200}$ relation, with a suite of cosmological simulations that include the effect of satellite depletion by the disc, we ask afresh whether there is, in fact, a missing satellite problem in the Milky Way in Λ CDM.

This paper is organised as follows. In §2, we describe the data used in this work. In §3, we describe the cosmological ‘zoom’ simulations of Milky Way mass halos that we use in this work to compare with our empirically derived subhalo mass function. In §4, we describe our $\langle \text{SFR} \rangle - M_{200}$ abundance matching method (§4.1, §4.3), and we describe our method for obtaining the $\langle \text{SFR} \rangle$ and dynamical M_{200}^{dyn} for a sample of isolated and satellite dwarfs (§4.4). In §5 we present our results. In §5.1, we compare M_{200}^{abund} derived from our $\langle \text{SFR} \rangle$ abundance matching with M_{200}^{dyn} for a sample of 11 isolated and 10 satellite dwarfs. In §5.3, we use the $\langle \text{SFR} \rangle - M_{200}$ relation to calculate the cumulative subhalo mass function of the Milky Way. We compare this to the simulations described in §3. In §6, we discuss the caveats and systematic errors inherent in our methodology, the implications of our results for other small scale puzzles in Λ CDM, and reionisation. Finally, in §7, we present our conclusions.

2 THE DATA

In this section, we describe the data used in this work. We construct the $\langle\text{SFR}\rangle - M_{200}$ relation using the Blanton et al. (2005) survey of low luminosity galaxies that had their stellar masses calculated by Baldry et al. (2008), as described in §4.3, augmented with data from Bauer et al. (2013) and Hill et al. (2017), as described in §4. This stellar mass function is complete down to $M_* \sim 2 \times 10^7 M_\odot$ (e.g. Read et al. 2017). To test the assumptions that go into building this relation, we compare it to measurements of $\langle\text{SFR}\rangle$ and M_{200}^{dyn} for a sample of 21 nearby dwarf galaxies. The 11 dwarf irregular (dIrr) galaxies are a subset of galaxies in the Little THINGS survey (Oh et al. 2015), chosen according to the selection criteria outlined in Iorio et al. (2017) and Read et al. (2017). We calculate $\langle\text{SFR}\rangle$ and M_{200}^{dyn} for this sample of dIrrs as described in §4.4. The satellite dwarf sample comprises the eight Milky Way ‘classical’ dwarf spheroidals (dSphs): Draco, Fornax, UMi, Carina, Sextans, Sculptor, Leo I, and Leo II, the Sagittarius dSph, and the Large Magellanic Cloud (LMC) that is a dwarf irregular. Our method for calculating M_{200}^{dyn} for this sample is described in §4.4. The stellar kinematic and photometric data required for mass modelling the classical dwarfs are taken from: Walker et al. (2009a) for Carina, Fornax, Sculptor and Sextans; Mateo et al. (2008) for Leo I; Spencer et al. (2017) for Leo II; Walker et al. (2015) for Draco; and Spencer et al., in prep. for Ursa Minor. The membership selection criteria and determination of the photometric light profiles for these galaxies is described in detail in Read et al. (2018).

To calculate the $\langle\text{SFR}\rangle$ for the above sample of galaxies, we require their star formation histories and stellar masses. For galaxies with continuing star formation today, we calculate $\langle\text{SFR}\rangle$ using equation 4 (see §4.4). We take stellar masses for the dIrr sample from Zhang et al. (2012) as in Read et al. (2017). For the sample of nearby satellite galaxies, we take M_* from the McConnachie (2012) review. In both cases, we assume errors on M_* of 25% (e.g. Mobasher et al. 2015). For the quenched satellites, we require also their star formation histories. For these, we use literature determinations derived from deep resolved colour magnitude diagrams (Draco, Aparicio et al. 2001; Sculptor, de Boer et al. 2012a; Carina, de Boer et al. 2014; Fornax, de Boer et al. 2012b; Sextans, Lee et al. 2009; UMi, Carrera et al. 2002; Leo I, Dolphin 2002; Leo II, Dolphin 2002; and Sagittarius, de Boer et al. 2015). In Appendix A, we also use the star formation histories of WLM and Aquarius to further test our methodology. We take these from Dolphin (2000) and Cole et al. (2014), respectively. Our full data compilation and derived M_{200}^{abund} and M_{200}^{dyn} for our sample of satellite dwarfs is reported in Table 1.

Finally, in §5.3, we also calculate M_{200}^{abund} estimates for the volume-incomplete sample of ‘ultra-faint’ dwarfs compiled in McConnachie (2012): Segue I, Ursa Major II, Bootes II, Segue II, Wilman I, Coma Berenices, Bootes III, Bootes I, Ursa Major, Hercules, Leo IV, Canes Venatici II, Leo V, Pices II and Canes Venatici I (and see Belokurov et al. 2007; Ibata et al. 2007; McConnachie 2012). Including these ultra-faint dwarfs is complicated by the fact that their star formation histories are more poorly measured than the classical dwarfs. They are also only detectable within the small survey footprint of the Sloan Digital Sky Survey (SDSS),

meaning that they are a lower bound on the total number within 280 kpc (e.g. Tollerud et al. 2008). Indeed, a large number of dwarfs have recently been found in the Dark Energy Survey (DES) data (Bechtol et al. 2015; Drlica-Wagner et al. 2015; Koposov et al. 2015). However, their uncertain relationship with the Magellanic Group makes it unclear whether or not they should be included in the census of Milky Way dwarfs (Jethwa et al. 2016). To be conservative, we include only those ultra-faints listed above and we apply *no volume completeness correction*. As such, when including the ultra-faints, our subhalo mass function will be a robust lower bound. Since the SFH of the ultra-faints is poorly constrained, we obtain an upper and lower bound on their $\langle\text{SFR}\rangle$ using equation 1, assuming that they formed all of their stars between 0.1 – 1 Gyrs after the Big Bang (Brown et al. 2012; Weisz et al. 2014).

3 THE SIMULATIONS

In §5, we compare our empirically derived cumulative subhalo mass function with expectations from ΛCDM using a suite of pure dark matter zoom-in simulations of Milky Way-like galaxies. These simulations were run with the N -body part of GADGET-3, which is an updated version of GADGET-2 (Springel 2005). The simulations are described in detail in Jethwa et al. (2018) but we briefly describe their general properties below.

We select 10 isolated Milky Way-like halos with virial masses between $M_{200} = 7.5 \times 10^{11} M_\odot$ and $M_{200} = 2 \times 10^{12} M_\odot$. For each halo, we perform a zoom-in simulation with a particle mass of $2.27 \times 10^5 M_\odot$ in the most refined region (enough to resolve subhaloes down to pre-infall masses of $M_{200} \sim 5 \times 10^7 M_\odot$; Power et al. 2003; Klypin et al. 2011). We then perform a second zoom-in simulation where a Miyamoto-Nagai disc potential (Miyamoto & Nagai 1975) is grown in the centre of the main halo between $z = 3$ and $z = 1$ (see Jethwa et al. 2018, for more details). The final disk has a mass of $8 \times 10^{10} M_\odot$, a scale radius of 3 kpc, and a scale height of 300 pc.

Recent comparisons between cosmological hydrodynamical zoom-ins and dark matter only zoom-ins in which disc potentials are grown have shown that including the disc potential accurately accounts for the destruction of subhalos (Garrison-Kimmel et al. 2017b). Furthermore, Bauer et al. (2018) found that the effect of the disc on substructure is the same if the disc is modelled as a potential or if it is simulated with particles and allowed to respond to the substructure. Thus, we have a set of 10 Milky Way-like halos where we can explore the amount of substructure and how it is affected by the inclusion of the disc.

We find that the disc results in a factor of 2 depletion in the amount of substructure within 100 kpc and a factor of 2 – 4 depletion within 30 kpc (depending on the mass of the main halo). We also find that this depletion is independent of subhalo mass. This suppression of subhalos broadly agrees with full hydrodynamical simulations in ΛCDM (e.g. Sawala et al. 2017; Garrison-Kimmel et al. 2017b) as well as previous works which have grown disks within cosmological simulations (D’Onghia et al. 2010).

Galaxy	Type	D (kpc)	M_* ($10^6 M_\odot$)	M_{gas} ($10^6 M_\odot$)	$\langle \text{SFR} \rangle$ ($M_\odot \text{ yr}^{-1}$)	M_{200}^{abund} ($10^9 M_\odot$)	M_{200}^{dyn} ($10^9 M_\odot$)	Refs.
UMi	dSph	76 ± 3	0.29	–	2.3×10^{-4}	2.8 ± 1.1	$2.2^{+1.1}_{-0.6}$	3,5
Draco	dSph	76 ± 6	0.29	–	1.2×10^{-4}	1.8 ± 0.7	$3.5^{+1.5}_{-1.0}$	3,4
Sculptor	dSph	86 ± 6	2.3	–	6.8×10^{-4}	5.7 ± 2.3	$3.6^{+1.9}_{-1.4}$	3,6
Sextans	dSph	86 ± 4	0.44	–	1.3×10^{-4}	2.0 ± 0.8	$1.0^{+0.6}_{-0.4}$	3,7
Leo I	dSph	254 ± 15	5.5	–	6.6×10^{-4}	5.6 ± 2.2	$1.8^{+1.2}_{-0.7}$	3,8
Leo II	dSph	233 ± 14	0.74	–	9.8×10^{-5}	1.6 ± 0.7	$1.1^{+0.8}_{-0.4}$	3,8
Carina	dSph	105 ± 6	0.38	–	3.4×10^{-5}	0.8 ± 0.3	$1.2^{+0.7}_{-0.5}$ ($0.4^{+0.4}_{-0.2}$)	3,9,16
Fornax	dSph	138 ± 8	43	–	5×10^{-3}	21.9 ± 7.4	$2.4^{+0.8}_{-0.5}$	3,10
Sagittarius	dSph	26 ± 2	121.5	–	1.7×10^{-2}	50.7 ± 13.3	> 60	3,11,12,14
SMC	dIrr	64 ± 4	460	460	3.3×10^{-2}	77.3 ± 16.9	–	3
LMC	dIrr	51 ± 2	2,700	460	2.0×10^{-1}	198.8 ± 34.3	250^{+90}_{-80}	3,13,15

Table 1. Data for the satellite dwarf galaxies that we study in this work. From left to right, the columns give: the name of the galaxy; type; distance from the centre of the Milky Way; stellar mass; gas mass (for the dIrrs); $\langle \text{SFR} \rangle$, derived using equation 4 for the dIrrs and equation 1 for the dSphs; M_{200}^{abund} derived from the $\langle \text{SFR} \rangle - M_{200}$ relation; M_{200}^{dyn} derived as described in §4.4; and data references. For Carina, M_{200}^{dyn} from the ‘disequilibrium modelling’ analysis of Ural et al. (2015) is quoted in brackets for comparison. The data references for each galaxy are as follows: 1: Read et al. (2017); 2: Dolphin (2000); 3: McConnachie (2012); 4: Aparicio et al. (2001); 5: Carrera et al. (2002); 6: de Boer et al. (2012a); 7: Lee et al. (2009); 8: Dolphin (2002); 9: de Boer et al. (2014); 10: de Boer et al. (2012b); 11: Niederste-Ostholt et al. (2012); 12: de Boer et al. (2015); 13: van der Marel (2006); 14: Gibbons et al. (2017); 15: Peñarrubia et al. (2016); 16: Ural et al. (2015).

4 METHOD

In this section, we describe our method for obtaining the $\langle \text{SFR} \rangle - M_{200}$ relation. We start by carefully defining the $\langle \text{SFR} \rangle$ (§4.1). We then explain how we obtain the cumulative $\langle \text{SFR} \rangle$ number density function of galaxies: $N_{\langle \text{SFR} \rangle}$, using data from the Sloan Digital Sky Survey (SDSS; Blanton et al. 2005; Hill et al. 2017) and the GAMA survey (Bauer et al. 2013; §4.2). In §4.3, we explain how we obtain the $\langle \text{SFR} \rangle - M_{200}$ relation from $N_{\langle \text{SFR} \rangle}$ using the Bolshoi simulation (Klypin et al. 2011). Finally, in §4.4 we describe how we obtain stellar masses, M_* , the $\langle \text{SFR} \rangle$, and dynamical masses, M_{200}^{dyn} , for individual satellite and central dwarf galaxies. In §5.1, we will use these to validate our $\langle \text{SFR} \rangle - M_{200}$ relation.

4.1 Defining the $\langle \text{SFR} \rangle$

We define the $\langle \text{SFR} \rangle$ as the star formation rate averaged over all times when a galaxy was actively forming stars. For individual galaxies where a measurement of the star formation rate as a function of time, $\text{SFR}(t)$ is available, this is:

$$\langle \text{SFR} \rangle = \frac{\int_0^{t_{\text{univ}}} f \cdot \text{SFR}(t) dt}{\int_0^{t_{\text{univ}}} f dt} \quad (1)$$

where $t_{\text{univ}} = 13.8$ Gyrs is the age of the Universe and:

$$f(t) = \begin{cases} 1 & \text{if } \text{SFR}(t) > \max[\text{SFR}]/3 \\ 0 & \text{otherwise} \end{cases} \quad (2)$$

The cut on $\text{SFR}(t) > \max[\text{SFR}]/3$ is chosen to avoid the $\langle \text{SFR} \rangle$ being biased low by periods where the SFR is slowly declining due to quenching. Our results are not sensitive to this choice.

We ensure that the $\text{SFR}(t)$ is normalised such that:

$$\int_0^{t_{\text{univ}}} \text{SFR}(t) dt = M_* \quad (3)$$

Notice that galaxies that have formed stars steadily for a Hubble time have $f \rightarrow 1$ and:

$$\langle \text{SFR} \rangle \rightarrow \frac{M_*}{t_{\text{univ}}} \quad (4)$$

while galaxies that have formed stars steadily and then quenched have $f \rightarrow 1 \forall \text{SFR}(t) \neq 0$ and:

$$\langle \text{SFR} \rangle \rightarrow \frac{M_*}{t_*} \quad (5)$$

where $t_* < t_{\text{univ}}$ is the total star formation time.

Thus, with the above definition of the $\langle \text{SFR} \rangle$, we only actually use the $\text{SFR}(t)$ to determine *when* (if ever) star formation was quenched. This is advantageous because the error on $\langle \text{SFR} \rangle$ is then determined primarily by the error on M_* that is available for large samples of galaxies and that has an uncertainty of order $\sim 25\%$ (e.g. Zhang et al. 2012; Mobasher et al. 2015). By contrast, well-estimated $\text{SFR}(t)$ are only available for a few nearby galaxies with deep colour

magnitude diagrams¹ (CMDs; e.g. Walcher et al. 2011; Ruiz-Lara et al. 2015). Furthermore, while $\text{SFR}(t)$ determined from SED fitting are available for a much larger sample of galaxies, the errors on the $\langle\text{SFR}\rangle$, determined in this way, are substantially larger than the errors on M_* (e.g. Zhang et al. 2012).

4.2 Obtaining the cumulative $\langle\text{SFR}\rangle$ number density function of galaxies

The cumulative $\langle\text{SFR}\rangle$ number density function of galaxies, $N_{\langle\text{SFR}\rangle}$, is the number of galaxies, N , with a $\langle\text{SFR}\rangle$ less than some value, normalised to a volume of 1 Mpc:

$$N_{\langle\text{SFR}\rangle} \equiv N(< \langle\text{SFR}\rangle) \quad (6)$$

We obtain this, as follows. First, we require the cumulative stellar mass number density function of galaxies, $N_* \equiv N(< M_*)$. For this, we use the redshift zero determination from Baldry et al. (2008) and Behroozi et al. (2013) which was derived from the Blanton et al. (2005) survey of low luminosity galaxies as part of the on-going SDSS survey campaign. This is shown in Figure 1, bottom panel (black band, where the width of the band represents the 68% confidence interval). For comparison, on this same panel we show N_* obtained from the GAMA survey, augmented with data from the G10-COSMOS survey (Davies et al. 2015; Wright et al. 2017; purple band). Notice that this is in excellent agreement with the N_* that we use in this work (black band), albeit with larger uncertainties due to the smaller survey volume (see Read et al. 2017 for a discussion of this). This suggests that our results are not sensitive to our choice of N_* determination. As discussed in §2, the stellar mass function that we use is complete down to $M_* \sim 2 \times 10^7 M_\odot$; below this stellar mass, we assume that dN_*/dM_* is described by a power law with an exponent of -1.6 .

Next, we split N_* into star forming and quenched galaxies (c.f. Peng et al. 2010). For this, we use the fraction of star forming galaxies as a function of stellar mass obtained from the GAMA survey by Bauer et al. (2013). This is shown in the top panel of Figure 1 (purple filled circles). We fit a smooth functional form to these data:

$$g = \left[\frac{1 - \tanh(\log_{10}[M_*/M_\odot] - \alpha)}{2} \right]^\beta \quad (7)$$

where $\alpha = 10.46$ and $\beta = 1.24$ are fitting parameters. This fit is shown by the smooth blue line in the top panel of Figure 1. The fraction of quenched galaxies is then given by $1 - g$, which is shown by the red smooth line. Applying equation 7 to the stellar mass function, dN_*/dM_* , and integrating, we obtain the cumulative stellar mass function of star forming and quenched galaxies. These are marked on Figure 1, bottom panel, by the blue and red bands, respectively.

Having split N_* into star forming and quenched populations, we can now estimate $\langle\text{SFR}\rangle$ for each population and

¹ Note that the closest of these have data for only small portions of the galaxy, requiring an extrapolation to determine the global $\langle\text{SFR}\rangle$ that we require here (e.g. Weisz et al. 2014; Bermejo-Clement et al. 2018).

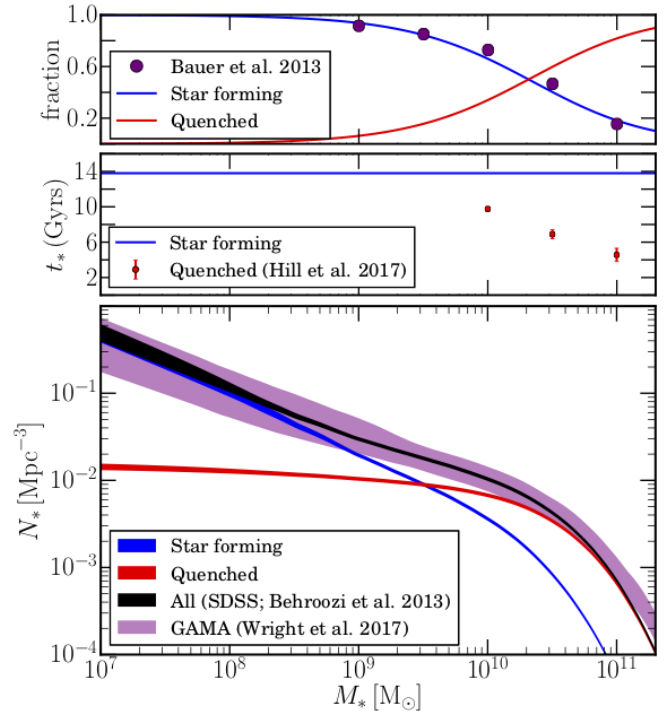


Figure 1. Top: The fraction of star forming galaxies as a function of stellar mass, M_* (purple data points, taken from Bauer et al. 2013). The blue line shows a fit to these data using equation 7; the red line shows the similar fraction of quenched galaxies. **Middle:** The total star formation time, t_* , as a function of M_* . For currently star forming galaxies, we assume $t_* = t_{\text{univ}} = 13.8$ Gyrs, which is marked by the horizontal blue line. For quenched galaxies, we linearly interpolate the data from Hill et al. (2017), marked by the red data points. **Bottom:** The cumulative stellar mass number density function of galaxies, N_* . The black band shows N_* for all galaxies, the blue band for star forming galaxies and the red band for quenched galaxies (as determined using the fraction of star forming and quenched galaxies shown in the top panel). The width of the bands shows the formal 68% confidence intervals. The purple band shows N_* determined using data from the GAMA survey, augmented with data from the G10-COSMOS survey (Davies et al. 2015; Wright et al. 2017). Notice that this is in excellent agreement with the N_* that we use in this work (black band), albeit with larger uncertainties due to the smaller survey volume.

then sum these to obtain $N_{\langle\text{SFR}\rangle}$. For the star forming population, we assume a star formation time $t_* = t_{\text{univ}}$ such that their $\langle\text{SFR}\rangle$ follows from equation 4. For the quenched population, we use the star formation time as a function of stellar mass, $t_*(M_*)$ estimated for galaxies using SDSS data by Hill et al. (2017). This is shown in the middle panel of Figure 1 by the red data points. (We linearly interpolate these data, assuming a constant $t_*(M_*)$ below $M_* = 10^{10} M_\odot$. Our results are not sensitive to these choices.) Also marked on this panel is the assumed star formation time for the star forming population $t_* = t_{\text{univ}}$ (horizontal blue line). With this estimate of $t_*(M_*)$, we obtain the $\langle\text{SFR}\rangle$ for the quenched galaxies using equation 5, folding the uncertainties on $t_*(M_*)$ into our estimate of $N_{\langle\text{SFR}\rangle}$. Note that, since $t_*(M_*)$ monotonically falls with M_* , $\langle\text{SFR}\rangle(M_*)$ for the quenched galaxies

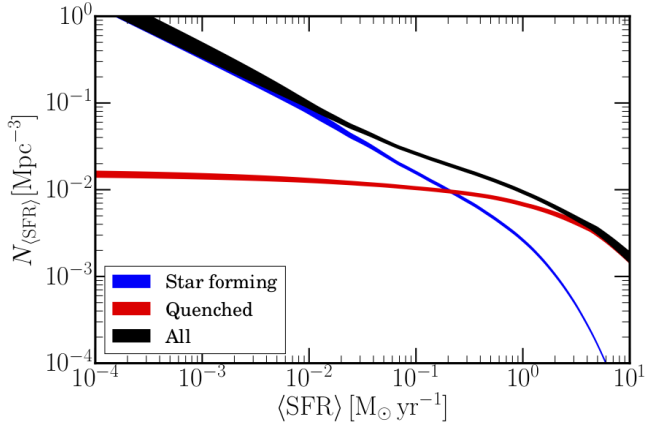


Figure 2. The cumulative $\langle \text{SFR} \rangle$ number density function of galaxies, $N_{\langle \text{SFR} \rangle}$. The black band shows $N_{\langle \text{SFR} \rangle}$ for all galaxies, the blue band for star forming galaxies and the red band for quenched galaxies. The width of the bands shows the formal 68% confidence intervals.

must *monotonically rise*. This key point makes the calculation substantially easier as we need not worry about galaxies with different M_* having the same $\langle \text{SFR} \rangle$.

In Figure 2, we show the $N_{\langle \text{SFR} \rangle}$ derived in the above way for the star forming (blue band) and quenched populations (red band), and their sum (black band). It is this latter that we will now use for abundance matching, next.

4.3 Abundance matching

Armed with our above estimate of $N_{\langle \text{SFR} \rangle}$, we are now in a position to use it for abundance matching. We perform this non-parametrically as in Read et al. (2017), using the dark matter halo mass function from the Λ CDM ‘Bolshoi’ simulation (Klypin et al. 2011). This assumes a Hubble parameter, $H_0 = 70 \text{ Mpc}^{-1} \text{ km s}^{-1}$; a ratio of the matter and dark energy density to the critical density of $\Omega_M = 0.27$ and $\Omega_\Lambda = 0.73$, respectively; a tilt of the power spectrum of $n = 0.95$ and the amplitude of the power spectrum on a scale of $8h^{-1} \text{ Mpc}$ of $\sigma_8 = 0.82$ (see e.g. Peacock 1999, for a full definition of these parameters). The Bolshoi simulation is accurate to $M_{200} \sim 10^{10} M_\odot$; below this mass scale we assume that the differential mass function, dN/dM_{200} , is a power-law with exponent -1.91 , consistent with higher resolution smaller-box cosmological N -body simulations (e.g. Reed et al. 2007). Similarly, the stellar mass function that we use here is only complete down to $M_* \sim 2 \times 10^7 M_\odot$ (see §2). Thus, $N_{\langle \text{SFR} \rangle}$ is only complete down to $\langle \text{SFR} \rangle \sim 0.0014 M_\odot \text{ yr}^{-1}$. Below this $\langle \text{SFR} \rangle$ we obtain $N_{\langle \text{SFR} \rangle}$ from a power-law extrapolation of the stellar mass function, as described in §4.2. Our non-parametric abundance matching proceeds by numerically mapping $\langle \text{SFR} \rangle(N)$ to $M_{200}(N)$, to determine $\langle \text{SFR} \rangle(M_{200})$ – i.e. the $\langle \text{SFR} \rangle$ – M_{200} relation. This assumes that there is no intrinsic scatter in the $\langle \text{SFR} \rangle$ – M_{200} relation, which is, for the time-being, consistent with our data constraints from nearby dwarf galaxies (see Figure 3). For subhalos in the Bolshoi simulation, we use their peak (i.e. pre-infall) halo

mass. As discussed in Reddick et al. (2013) and Lehmann et al. (2017), abundance matching can be further improved by using instead the peak circular velocity of halos, v_{peak} , and by including some intrinsic scatter. This is particularly important for galaxy clustering (see also Hearin et al. 2013). We will explore such improvements in future work.

Recall that our $\langle \text{SFR} \rangle$ – M_{200} relation relies only on the assumptions that: (i) the $\langle \text{SFR} \rangle$ is monotonically related to M_{200} with little scatter; and (ii) that the Λ CDM cosmological model is correct. We will test these assumptions by comparing our $\langle \text{SFR} \rangle$ – M_{200} relation with estimates of $\langle \text{SFR} \rangle$ and M_{200} for a sample of 21 nearby dwarf galaxies in §5.1. We discuss, next, how we obtain M_* , $\langle \text{SFR} \rangle$ and a dynamical estimate of the peak M_{200} (that we will refer to as M_{200}^{dyn}) for these dwarfs.

4.4 Determining M_* , $\langle \text{SFR} \rangle$ and M_{200}^{dyn} for isolated and satellite dwarfs

To assess the validity of our $\langle \text{SFR} \rangle$ – M_{200} relation, in §5 we compare it with measurements of the $\langle \text{SFR} \rangle$ and a dynamical estimate of the pre-infall halo mass, M_{200}^{dyn} , for nearby dwarf galaxies. In this section, we describe our method for obtaining M_* , $\langle \text{SFR} \rangle$ and M_{200}^{dyn} for these dwarfs.

4.4.1 Determining M_* and $\langle \text{SFR} \rangle$

For M_* , we use the values reported in Read et al. (2017) for the isolated dwarf sample (which are taken from Zhang et al. 2012), and those in McConnachie (2012) for the satellite dwarfs. These are reported in Table 1. For the $\langle \text{SFR} \rangle$, we use equation 4 for our isolated dwarfs and equation 1 for the quenched satellites; all of these have $\text{SFR}(t)$ determined from deep CMDs. The $\text{SFR}(t)$ data that we use and our derived $\langle \text{SFR} \rangle$ for these dwarfs are given in §2 and Table 1.

4.4.2 Determining M_{200}^{dyn} for the dwarf spheroidals

For the gas-free Milky Way dwarf spheroidal (dSph) galaxies, we calculate a dynamical estimate of their pre-infall halo mass, M_{200}^{dyn} , by mass modelling their stellar kinematics and photometric light profile with the GRAVSPHERE code. GRAVSPHERE uses the Jeans equations to fit the line of sight velocities and photometric light profile of tracer stars, assuming only spherical symmetry and that the stars are in a steady state. The code is described and extensively tested on mock data in Read & Steger (2017) and Read et al. (2018), including tests on non-spherically symmetric mocks, tidally stripped mocks, and mocks that include foreground contamination and binary stars. Here, we use the code as in Read et al. (2018) where the dark matter mass profile is given by the CORENFWTIDES model:

$$\rho_{\text{cNFWt}}(r) = \begin{cases} \rho_{\text{cNFW}} & r < r_t \\ \rho_{\text{cNFW}}(r_t) \left(\frac{r}{r_t}\right)^{-\delta} & r > r_t \end{cases} \quad (8)$$

where ρ_{cNFW} is given by:

$$\rho_{\text{cNFWt}}(r) = f^n \rho_{\text{NFW}} + \frac{nf^{n-1}(1-f^2)}{4\pi r^2 r_c} M_{\text{NFW}} \quad (9)$$

and ρ_{NFW} and M_{NFW} are the ‘NFW’ density and mass profile given by (Navarro et al. 1996b):

$$\rho_{\text{NFW}}(r) = \rho_0 \left(\frac{r}{r_s} \right)^{-1} \left(1 + \frac{r}{r_s} \right)^{-2} \quad (10)$$

$$M_{\text{NFW}}(r) = M_{200} g_c \left[\ln \left(1 + \frac{r}{r_s} \right) - \frac{r}{r_s} \left(1 + \frac{r}{r_s} \right)^{-1} \right] \quad (11)$$

with scale length r_s :

$$r_s = r_{200}/c_{200} \quad (12)$$

where:

$$g_c = \frac{1}{\log(1 + c_{200}) - \frac{c_{200}}{1+c_{200}}} \quad (13)$$

and:

$$r_{200} = \left[\frac{3}{4} M_{200} \frac{1}{\pi \Delta \rho_{\text{crit}}} \right]^{1/3} \quad (14)$$

where c_{200} is the ‘concentration parameter’, $\Delta = 200$, $\rho_{\text{crit}} = 136.05 M_{\odot} \text{ kpc}^{-3}$ is the critical density of the Universe at redshift $z = 0$, r_{200} is the virial radius, and M_{200} is the virial mass.

The CORENFWTIDES model has six free parameters: M_{200} and c_{200} that are identical to the free parameters in the NFW model, r_c that controls the size of the central dark matter core, n that controls the inner logarithmic slope of the density profile ($n = 1$ is maximally cored, while $n = 0$ reverts to a cusped NFW profile), and r_t and δ that set the radius and outer density slope beyond which mass is tidally stripped from the galaxy, respectively. The CORENFWTIDES model allows us to fit directly for the pre-infall halo mass, M_{200} , while allowing for a central dark matter core and/or some outer steepening of the density profile due to tides, should the data warrant it. The only difference between the application of the CORENFWTIDES model to Draco in Read et al. (2018) and our analysis here is that in this paper we use slightly more generous priors on M_{200} and c_{200} : $8.5 < \log_{10}(M_{200}/M_{\odot}) < 10.5$; $9 < c_{200} < 24$; $-2 < \log_{10}(r_c/\text{kpc}) < 0.5$; $0.3 < \log_{10}(r_t/R_{1/2}) < 1$; and $3.5 < \delta < 5$. This is because we found that some of the dwarfs were pushing on the lower bound of the priors on M_{200} used in Read et al. (2018). As in Read et al. (2018), we fix $n = 1$.

4.4.3 Determining M_{200}^{dyn} for the dwarf irregulars

For the gas rich isolated dwarf irregulars (dIrrs), we use the dynamical estimate of the halo mass, M_{200}^{dyn} , determined for these galaxies previously in Read et al. (2017). We refer the reader to that work for the resulting M_{200}^{dyn} values, with uncertainties. For completeness, we briefly summarise the methodology used in that paper, below. The rotation curves were derived from HI datacubes using the publicly available software ^{3D}BAROLO (Di Teodoro & Fraternali 2015; Iorio et al. 2017). These were mass modelled by decomposing the circular speed curve into contributions from stars, gas and dark matter:

$$v_c^2 = v_*^2 + v_{\text{gas}}^2 + v_{\text{dm}}^2 \quad (15)$$

where v_* and v_{gas} are the contributions from stars and gas, respectively, and v_{dm} is the dark matter contribution. The stars and gas were assumed to be well-represented by thin exponential discs. The dark matter halo was assumed to be spherically symmetric with a CORENFW density profile (equation 9), with $n = 1$. For the fits, the scale lengths of the star and gas disc were held fixed. Read et al. (2017) assumed priors on the CORENFW model parameters of: $8 < \log_{10}[M_{200}/M_{\odot}] < 11$; $14 < c_{200} < 30$; and a flat linear prior on M_* over the range given by stellar population synthesis modelling. They showed that the resulting constraints on M_{200}^{dyn} are not sensitive to this choice of priors, nor the assumed mass model. The mass modelling methodology used in Read et al. (2017) was extensively tested on mock data in Read et al. (2016b), demonstrating that, with data of the quality available from the Little THINGS survey (see §2), they were able to obtain an unbiased estimate of M_{200}^{dyn} .

Finally, for the LMC and Sagittarius, we use M_{200}^{dyn} values from the literature. The pre-infall halo mass of the LMC was recently estimated by Peñarrubia et al. (2016) using a timing argument. They found $M_{200,\text{LMC}} = 0.25_{-0.08}^{+0.09} \times 10^{12} M_{\odot}$ (a similar estimate has been determined recently by Erkal et al. (2018) using an entirely different analysis that models the deflection of the Tucana III stream due to the recent close passage of the LMC). The Sagittarius dwarf’s pre-infall M_{200}^{dyn} was estimated by Gibbons et al. (2017) from the kinematics of its stellar stream stars. They found $M_{200,\text{Sag}} > 6 \times 10^{10} M_{\odot}$. These values are reported in Table 1.

5 RESULTS

5.1 Comparing the $\langle \text{SFR} \rangle - M_{200}$ relation with data for nearby isolated and satellite dwarfs

In this section, we test and validate our $\langle \text{SFR} \rangle - M_{200}$ relation by comparing it to data for a sample of 21 nearby dIrr and dSph galaxies, described in §2 and Table 1. Figure 3 shows the $M_* - M_{200}$ relation from Read et al. (2017) (solid blue lines, left) and the $\langle \text{SFR} \rangle - M_{200}$ relation, derived as described in §4.3 (solid blue lines, right). The lines become dashed where they rely on power law extrapolations of N_* (left pane) or $N_{\langle \text{SFR} \rangle}$ (right panel). The upper and lower lines delineate the formal 68% confidence regions for the $M_* - M_{200}$ and $\langle \text{SFR} \rangle - M_{200}$ relations, respectively. (These errors follow from the propagation of the errors in the cumulative stellar mass function (Figure 1) and do not include the systematic uncertainties.) Overplotted are data from the sample of 11 isolated dIrrs taken from Read et al. (2017) (purple data points) and the satellite dwarfs studied in this paper (black data points). The former have their M_{200}^{dyn} derived from their HI rotation curves (Read et al. 2017) and their $\langle \text{SFR} \rangle$ derived from their stellar masses (equation 4). The latter have their M_{200}^{dyn} and $\langle \text{SFR} \rangle$ determined as described in §4.4 (see also Table 1).

Firstly, notice that most of the satellite dwarfs (black) scatter below the $M_* - M_{200}$ relation (left panel), with the exception of Fornax. Draco and UMi lie more than a dex below, while Sagittarius is off by a factor ~ 3 . This is what we expect if the scatter owes to star formation being quenched on infall, as marked by the red arrow (and see §1). By

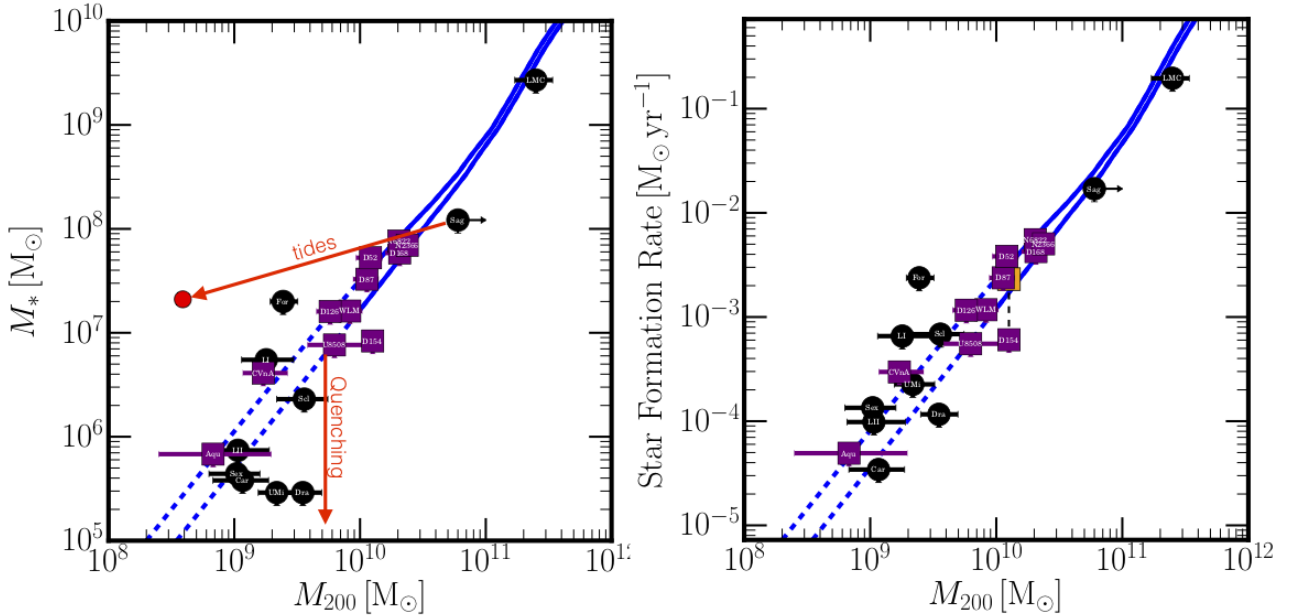


Figure 3. Abundance matching with the stellar mass, M_* (left), and the mean star formation rate, $\langle\text{SFR}\rangle$ (right). The blue lines show the $M_* - M_{200}$ relation from Read et al. (2017) (left) and the $\langle\text{SFR}\rangle - M_{200}$ relation, derived as described in §4.3 (right). The lines become dashed where they rely on power law extrapolations of N_* (left panel) or $N_{\langle\text{SFR}\rangle}$ (right panel). The upper and lower lines delineate the formal 68% confidence regions for the $M_* - M_{200}$ and $\langle\text{SFR}\rangle - M_{200}$ relations, respectively (see text for details). The purple data points show isolated dIrrs with M_{200}^{dyn} derived from their HI rotation curves (Read et al. 2017) and $\langle\text{SFR}\rangle$ derived from their stellar masses (equation 4). The black data points show satellite dwarfs. These have their M_{200}^{dyn} and $\langle\text{SFR}\rangle$ determined as described in §4.4 (and see Table 1). Notice that most of the satellites scatter below the $M_* - M_{200}$ relation (left); this owes to satellite quenching (red arrow, as marked). Fornax, however, lies above the relation, indicative of tidal stripping (see red arrow, as marked). Indeed, the present-day M_* and M_{200}^{dyn} for the Sagittarius dwarf (red) are significantly lower than estimates of its pre-infall M_* and M_{200}^{dyn} that utilise data from its tidal tails (black data point marked ‘Sag’, and see text for further details). The orange square, connected to DDO 154 by a dashed line in the right-panel, shows the location of DDO 154 if its *current* SFR is used instead of its Hubble time averaged $\langle\text{SFR}\rangle$ (see text for further details).

contrast, the scatter about the $\langle\text{SFR}\rangle - M_{200}$ relation (right panel) is significantly reduced. Now Sagittarius and UMi lie on the relation within their 68% confidence intervals, while Draco lies just outside the 68% lower bound on its M_{200}^{dyn} . This occurs because dwarfs like Draco have their star formation shut down on infall to the Milky Way, causing their M_* to be systematically low for their pre-infall M_{200} . Their $\langle\text{SFR}\rangle$, however, does not depend on when star formation is truncated and so correlates better with M_{200} than M_* does (see also Appendix A). Our key result for this paper is that our sample of 21 dwarfs is in excellent agreement with our derived $\langle\text{SFR}\rangle - M_{200}$ relation down to $M_{200} \sim 10^9 M_\odot$, even over the region $10^9 < M_{200}/M_\odot < 10^{10}$ that relies on a power law extrapolation of the $N_{\langle\text{SFR}\rangle}$ function to low $\langle\text{SFR}\rangle$ (see Figure 3, right panel, dashed blue lines). This validates our use of this power law extrapolation, at least down to $\langle\text{SFR}\rangle \sim 10^{-4} M_\odot \text{ yr}^{-1}$. We discuss this further in §6.

While most of the satellites scatter below the $M_* - M_{200}$ relation, Fornax lies significantly above and remains an outlier also in the $\langle\text{SFR}\rangle - M_{200}$ relation (Figure 3). This could indicate that Fornax lost significant mass due to tides. Tidal mass loss lowers M_{200}^{dyn} at a fixed M_{200}^{abund} (see §1). If sufficient mass loss occurs, M_* will start to be lowered also, forming visible tidal tails. To test whether this could explain Fornax’s position in the $M_* - M_{200}$ and $\langle\text{SFR}\rangle - M_{200}$ plots, we consider the Sagittarius dwarf that is known to be tidally

disrupting today (Ibata et al. 1995, 1997). The red circle in Figure 3 (left panel) marks the location of Sagittarius in the $M_* - M_{200}$ plot if we use its present-day stellar mass (McConnachie 2012) and M_{200}^{dyn} (we estimate this using Sagittarius’ current stellar kinematics (Ibata et al. 1997) and the Jeans mass estimator from Walker et al. (2009b)). Notice that these ‘present-day’ M_* and M_{200}^{dyn} are lower than our default estimates. This is because our default estimate for M_* corrects for stellar mass loss using Sagittarius’ prominent tidal tails (Niederste-Ostholt et al. 2010, 2012), while our default M_{200}^{dyn} is calculated from the dynamics of Sagittarius stream stars, giving a lower bound on its *pre-infall* halo mass (Gibbons et al. 2017). Thus, for Sagittarius, we see evidence that tides have lowered both its M_{200}^{dyn} and M_* after infall (see the red arrow marked ‘tides’ in Figure 3, left panel). (Indeed, Helmi & White (2001) use dynamical models of Sagittarius disrupting in the Milky Way to show that it likely lost significant mass after accreting onto our Galaxy.) Like Sagittarius, Fornax may have lowered its M_{200}^{dyn} through tides. We note, however, that such an explanation may be challenging to reconcile with Fornax’s apparently near-circular orbit (Lux et al. 2010; Battaglia et al. 2015; Gaia Collaboration et al. 2018) and lack of evident tidal tails (e.g. Bate et al. 2015). We will explore this further in future work.

Finally, there is one more significant outlier in the

(SFR)– M_{200} relation (Figure 3, right panel): DDO 154 (marked D154). Uniquely amongst the dIrrs that we consider here, DDO 154 is currently forming stars at four times its $\langle \text{SFR} \rangle$ averaged over a Hubble time (Zhang et al. 2012). It also has an unusually high HI gas fraction of $M_{\text{HI}}/M_* = 37$ (Read et al. 2017). As noted by Read et al. (2017), at its currently observed star formation rate of $\dot{M}_* = 4.3 \times 10^{-3} M_\odot \text{yr}^{-1}$ (Zhang et al. 2012), DDO 154 would move onto the $M_* - M_{200}$ relation in ~ 5.7 Gyrs. This may indicate that it has recently undergone a major merger that increased both its M_{200} and its SFR, but has not yet increased its M_* . Indeed, if we use DDO 154’s current SFR, rather than its $\langle \text{SFR} \rangle$, DDO 154 moves onto the $\langle \text{SFR} \rangle$ – M_{200} relation (see the orange data point in Figure 3 that is connected to DDO 154 by a dashed line).

5.2 Using the $\langle \text{SFR} \rangle$ – M_{200} relation to estimate pre-infall halo masses

In Figure 4, we compare $M_{200}^{\text{abund}^*}$ – derived from the standard $M_* - M_{200}$ abundance matching relation (left), and our new $\langle \text{SFR} \rangle$ – M_{200} relation (right) – with M_{200}^{dyn} for our dwarf sample (see §2). As can be seen, when using standard abundance matching with M_* (left), the satellite dwarfs (black) show a large scatter around the dashed line that marks $M_{200}^{\text{dyn}} = M_{200}^{\text{abund}^*}$. By contrast, when using our new $\langle \text{SFR} \rangle$ – M_{200} relation (right), the satellites show much less scatter. Now most of the dwarfs – *whether isolated or a satellite* – have a M_{200}^{dyn} and M_{200}^{abund} that agree within their 68% confidence intervals. Only Fornax and DDO154 (discussed in §5.1, above) remain as significant outliers. To quantify this improvement, we define a χ^2 statistic:

$$\chi^2 = \sum_{i=0}^N \frac{(M_{200,i}^{\text{abund}} - M_{200,i}^{\text{dyn}})^2}{(\sigma_i^{\text{abund}})^2 + (\sigma_i^{\text{dyn}})^2} \quad (16)$$

where σ_i^{abund} is the uncertainty on $M_{200,i}^{\text{abund}}$ (or $M_{200,i}^{\text{abund}^*}$) for a given dwarf, i , and similarly for the other quantities. Evaluating equation 16 over all $N = 7$ dwarfs with truncated star formation (Draco, UMi, Sextans, Leo I, Leo II, Sagittarius and Sculptor), we obtain $\chi^2 = 7$ when abundance matching with the $\langle \text{SFR} \rangle$, and $\chi^2 = 25$ for abundance matching with M_* .

As a final check of our methodology, we note that the Carina dSph has an independent estimate of its pre-infall M_{200}^{dyn} from ‘disequilibrium modelling’. Ural et al. (2015) directly fit a large ensemble of N -body models to both its internal stellar kinematic data and extra-tidal stars far from the centre of the dwarf, finding $M_{200,\text{Car}} = 3.6_{-2.3}^{+3.8} \times 10^8 M_\odot$ at 68% confidence. This is in excellent agreement with both the M_{200}^{abund} and M_{200}^{dyn} that we derive for Carina here (see Table 1 and Figure 4).

5.3 The cumulative subhalo mass function of the Milky Way

In this section, we now use our $\langle \text{SFR} \rangle$ – M_{200} relation to obtain an empirical estimate of the subhalo mass function of the Milky Way. For this, we use the volume complete sample of dwarfs within 280 kpc of the Galactic centre, described in §2. We augment these with a volume-incomplete sample

of ‘ultra-faint’ dwarfs. These latter are a lower bound on the total number of ultra-faints since we do not perform any volume incompleteness correction, nor do we include any of the new discoveries in the Dark Energy Survey (see §2 for a discussion of these choices). To illustrate how our new $\langle \text{SFR} \rangle$ – M_{200} relation changes the results, we repeat our analysis using the more familiar $M_* - M_{200}$ relation. As shown in §5.1, the $M_* - M_{200}$ relation is not valid for quenched satellites, but, as we shall see, this comparison is nonetheless helpful for understanding our results.

Figure 5 shows the cumulative pre-infall subhalo mass mass function of the Milky Way within 280 kpc, derived using the $M_* - M_{200}$ relation (left) and our new $\langle \text{SFR} \rangle$ – M_{200} relation (right). The blue lines show the median (solid) and $\pm 68\%$ confidence intervals (dashed) for just the volume-complete classical dwarfs (see §2). The contribution of each dwarf to the cumulative number density is marked by the labels. The green lines show the same but including the sample of ultra-faint dwarfs from McConnachie (2012). (Recall that this is a *lower bound* on the total number of ultra-faints.) The grey shaded region shows the spread in $N(< M_{200})$ of ten pure-dark matter Milky Way zoom simulations in Λ CDM (see §3). The red shaded region shows the same, but including a model for the stellar disc of the Milky Way. This increases the tidal disruption of satellites on plunging orbits causing the subhalo mass function to shift to lower masses (see §3). In both cases, the subhalo masses, M_{200} , are defined to be their peak mass before infall.

From Figure 5, we can see that when abundance matching with the $M_* - M_{200}$ relation (left), the Milky Way dwarfs inhabit low mass subhalos. In this case, there is a severe missing satellites problem below $M_{200} \sim 2 \times 10^9 M_\odot$: the Milky Way does not contain enough galaxies like Sculptor or Leo I to be consistent with the Λ CDM models. This is a severe problem because we already have a complete census of dwarfs this bright (e.g. Koposov et al. 2008). However, as shown in §5.1, the $M_* - M_{200}$ relation should not be applied to quenched satellites. Using instead our new $\langle \text{SFR} \rangle$ – M_{200} relation (right) places the dwarfs in higher mass subhalos and alters their mass-ordering. Now the Milky Way’s cumulative subhalo mass function sits comfortably within the range of models (red shaded region) down to $M_{200} \sim 10^9 M_\odot$. Below this mass scale, the subhalos are inhabited by the ultra-faint dwarfs (green lines), for which we do not have yet a complete census. As a result, we are not yet able to say whether or not there is a ‘missing satellites’ problem below $M_{200} \sim 10^9 M_\odot$ in the Milky Way.

Finally, note that our analysis places the ultra-faints in dark matter halos with pre-infall halo masses in the range $M_{200} \sim 5 \times 10^8 - 5 \times 10^9 M_\odot$. This is in good agreement with other recent studies (e.g. Kim et al. 2017; Jethwa et al. 2018) and dynamical estimates (e.g. Contenta et al. 2017). Below $M_{200} \sim 5 \times 10^8 M_\odot$ the Milky Way is either truly devoid of visible satellites, or such low mass halos contain just a few tens to hundreds of stars. If this latter is the case, some of these low mass satellites may be detected by the Gaia satellite (e.g. Antoja et al. 2015; Ciucă et al. 2018).

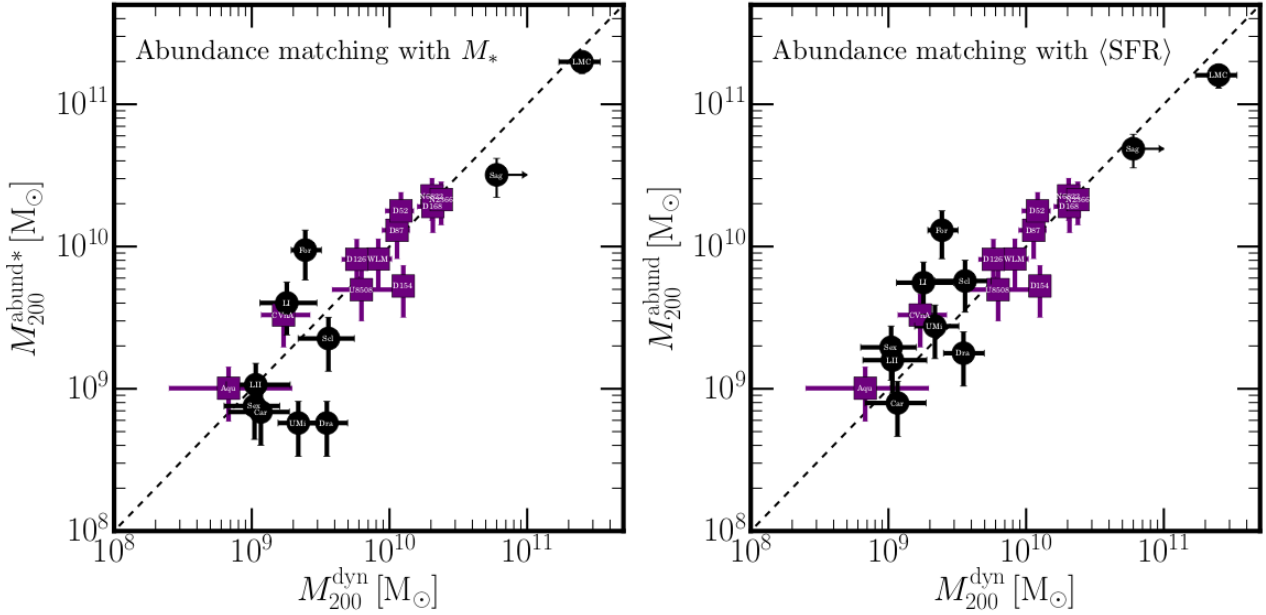


Figure 4. A comparison of the pre-infall $M_{200}^{\text{abund*}}$ – derived using standard abundance matching with M_* (left), and our new $\langle\text{SFR}\rangle$ – M_{200} abundance matching (right) – with dynamical estimates for nearby galaxies, M_{200}^{dyn} . The purple data points show the sample of isolated star forming dwarf irregulars from (Read et al. 2017); these have their M_{200}^{dyn} estimated from their HI rotation curves. The black points show our sample of Milky Way satellite galaxies (§2). These have their M_{200}^{dyn} estimated as described in §4.4. The dashed lines mark $M_{200}^{\text{dyn}} = M_{200}^{\text{abund*}}$ and $M_{200}^{\text{dyn}} = M_{200}^{\text{abund}}$, respectively. Notice that the scatter in M_{200}^{abund} is reduced as compared to $M_{200}^{\text{abund*}}$. To quantify this improvement, we define a χ^2 statistic in equation 16. With this, we obtain $\chi^2 = 7$ when abundance matching with the $\langle\text{SFR}\rangle$, and $\chi^2 = 25$ for abundance matching with M_* .

6 DISCUSSION

6.1 Caveats and gremlins

In this section, we discuss the assumptions inherent in our methodology, and likely sources of systematic uncertainty. Firstly, while our sample of classical dwarfs is volume complete down to a given *stellar mass*, this does not mean that it is volume complete down to a given *halo mass*. Thus, we may expect, particularly as we approach $10^9 M_\odot$, that our cumulative mass function is a lower bound, even if using just the classical dwarfs. Indeed, adding in the sample of ultra-faint dwarfs from McConnachie (2012) we saw exactly this behaviour, with a substantial increase in $N(< M_{200})$ at $M_{200} \sim 10^9 M_\odot$ (compare the blue and green lines in Figure 5, right panel). Secondly, the $\langle\text{SFR}\rangle$ – M_{200} relation relies on a power law extrapolation of $N_{\langle\text{SFR}\rangle}$ below $\langle\text{SFR}\rangle \sim 0.0014 M_\odot \text{ yr}^{-1}$ (see dashed blue lines in Figure 3, right panel). In §5, we argued that this extrapolation is justified by the fact that our sample of 21 dwarf galaxies gives a good match to the $\langle\text{SFR}\rangle$ – M_{200} relation down to $M_{200} \sim 10^9 M_\odot$ (see Figure 3, right panel). Finally, we have only tested the $\langle\text{SFR}\rangle$ – M_{200} relation down to $M_{200} \sim 10^9 M_\odot$ (see Figure 4, right panel). At lower masses than this, there may be substantial scatter in the $\langle\text{SFR}\rangle$ – M_{200} relation, or a departure from our assumed power-law extrapolation of $N_{\langle\text{SFR}\rangle}$, that could cause our estimates of M_{200}^{abund} to become biased. This becomes important when applying our $\langle\text{SFR}\rangle$ – M_{200} relation to dwarfs with $\langle\text{SFR}\rangle \lesssim 10^{-4} M_\odot \text{ yr}^{-1}$.

6.2 How well can we determine M_{200}^{dyn} ?

In §5.2, we argued that M_{200}^{abund} gives a more reliable estimate of the pre-infall halo mass for quenched satellites than does $M_{200}^{\text{abund*}}$. However, this statement relies on our dynamical estimates of pre-infall halo masses, M_{200}^{dyn} . For our sample of isolated dwarf irregulars, we estimated this from their HI rotation curves, as described in §4.4.3; for the dSphs we used their line of sight stellar kinematics, as described in §4.4.2. For the dIrrs, our estimate of M_{200}^{dyn} is unlikely to be biased. They have not experienced any mass loss due to infall to a larger galaxy, while the HI rotation curve for almost all galaxies in our sample extends to the region where it becomes flat, significantly reducing the uncertainty on M_{200}^{dyn} (e.g. Read et al. 2016b, 2017). For the dSphs, however, determining M_{200}^{dyn} is more challenging. Firstly, we only have data out to a few stellar half light radii. This will increase the uncertainty on M_{200}^{dyn} , but should not introduce bias. Secondly, however, at least some of our sample of dSphs is likely to have suffered significant tidal stripping and shocking due to their orbits around the Milky Way. This acts to lower the inner density of the dwarf, biasing our estimate of M_{200}^{dyn} low (e.g. Read et al. 2006b). Indeed, the Sagittarius dwarf is known to be at an advanced stage of tidal disruption (Ibata et al. 1995, 1997). In §5.1, we showed that current estimates of M_{200}^{dyn} for Sagittarius are indeed biased low by a factor ~ 100 as compared to the estimate from the kinematics of Sagittarius’ tidal stream (see Figure 3). However, the remainder of our sample of dSphs is unlikely to have been strongly influenced by tides since they move on relatively benign orbits around the Milky Way (Read et al. 2006b; Lux

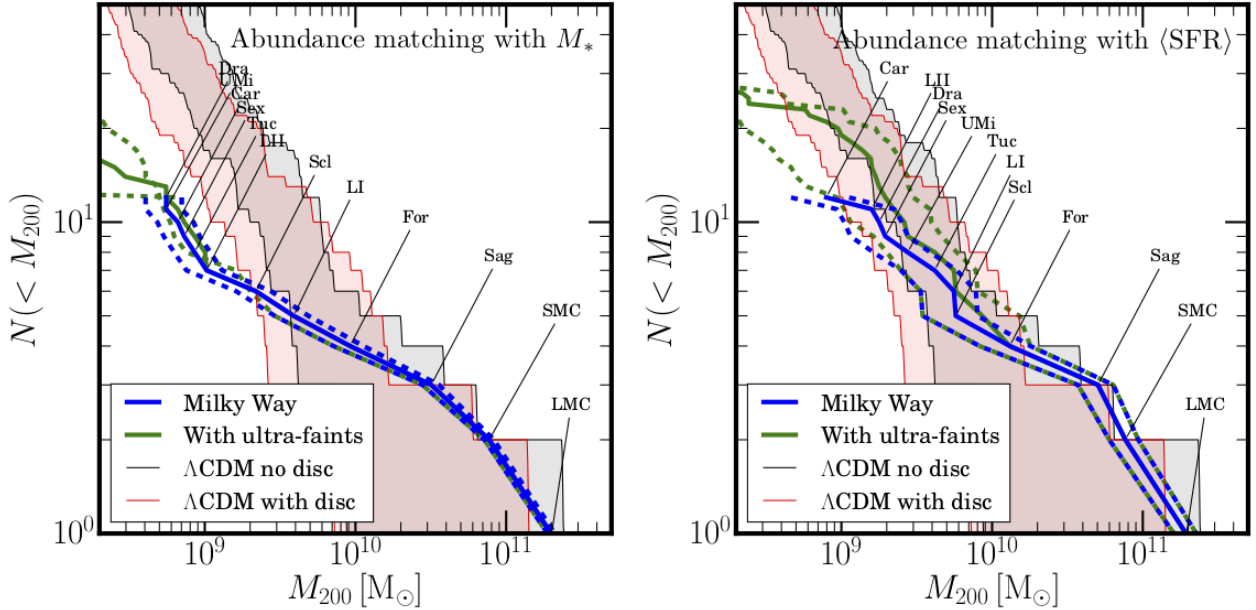


Figure 5. The cumulative subhalo mass function of the Milky Way within 280 kpc of the Galactic centre, determined using the $M_* - M_{200}$ relation (left) and the $\langle \text{SFR} \rangle - M_{200}$ relation (right). The names of the individual galaxies that contribute to the mass function are marked on the plot. The blue and blue dashed lines mark the median and $\pm 68\%$ confidence intervals, respectively. The green lines show the same but including the sample of ultra-faint dwarfs from McConnachie (2012). This is a *lower bound* on the total number of ultra-faints since we have not included the recent DES discoveries, nor accounted for their volume incompleteness within 280 kpc (see §2). The grey shaded region shows the spread in $N(< M_{200})$ of ten pure-dark matter Milky Way zoom simulations in ΛCDM (see §3). The red shaded region shows the same, but including a model for the stellar disc of the Milky Way. In both cases, the subhalo masses, M_{200} , are defined to be their peak mass before infall. Notice that, when abundance matching with the $M_* - M_{200}$ relation (left), the Milky Way dwarfs inhabit lower mass subhalos. In this case, there is a severe missing satellites problem below $M_{200} \sim 2 \times 10^9 M_\odot$. By contrast, the $\langle \text{SFR} \rangle - M_{200}$ relation places the dwarfs in higher mass subhalos and alters their mass-ordering (right). Now the Milky Way’s cumulative subhalo mass function sits comfortably within the range of models (red shaded region) down to $M_{200} \sim 10^9 M_\odot$.

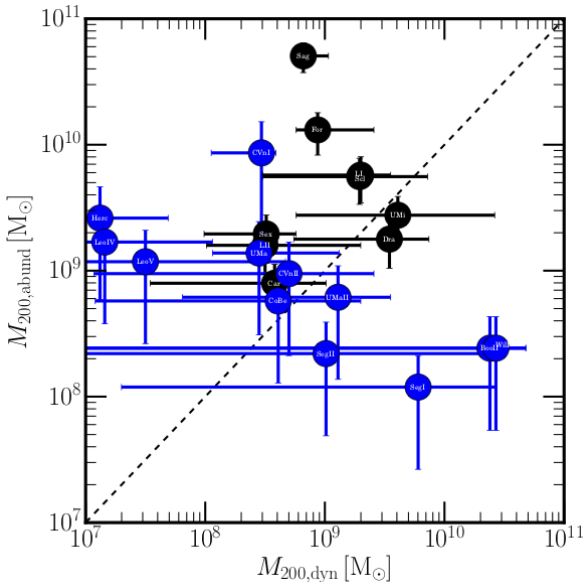


Figure 6. A comparison of M_{200}^{abund} derived in this paper with dynamical masses derived using the mass estimator from Errani et al. (2018). The Milky Way classical dSphs are marked in black, while the ultra-faint dwarfs are marked in blue.

et al. 2010; Read et al. 2018). Indeed, in §5.2 we showed that an independent estimate of M_{200}^{dyn} for the Carina dSph based on ‘disequilibrium modelling’ – that includes tidal effects (Ural et al. 2015) – was in excellent agreement with the estimate of M_{200}^{dyn} for Carina presented here.

As a final test, we compare our estimates of M_{200}^{dyn} for the dSphs with an unbiased estimator developed recently by Errani et al. (2018). This was calibrated on the ‘Aquarius’ simulation (a pure dark matter N -body simulation of a Milky Way-mass galaxy in an ΛCDM cosmology; Springel et al. 2008). In Figure 6, we plot M_{200}^{dyn} from Errani et al. (2018) against M_{200}^{abund} derived in this paper for the Milky Way classical dSphs (black) and ultra-faint dwarfs (blue). Firstly, note that the Errani et al. (2018) estimator has much larger uncertainties on M_{200}^{dyn} than our GRAVSPHERE estimates (see Figure 4). This is because GRAVSPHERE takes full advantage of the photometric light profile and the second and fourth order moments of the velocity distribution (see §4.4). Nonetheless, the classical dSphs (black data points) broadly agree with our estimates of M_{200}^{abund} within their quoted uncertainties, with the exception of Sagittarius and Fornax. This is in good agreement with our results in Figures 3 and 4, where we found a similar discrepancy for these two dSphs that are likely affected by tides (see above). The ultra-faint dSphs (blue data points) have very large uncertainties on M_{200}^{dyn} . As a result, most are consistent with our M_{200}^{abund} estimates. However, CVnI, Leo IV, Leo V and Hercules all

have $M_{200}^{\text{dyn}} < M_{200}^{\text{abund}}$ at 68% confidence. This may indicate that, like Sagittarius and Fornax, these galaxies have had their masses lowered by tidal forces after infall to the Milky Way. We will explore this further in future work.

6.3 The missing satellites problem

There are many studies that have shown that the missing satellites problem can be solved by an appropriate mapping between visible satellites and subhalos (e.g. Madau et al. 2008; Boylan-Kolchin et al. 2012; Brook et al. 2014; Kim et al. 2017). However, what is new in this paper is that we have not actually set out to solve the missing satellites problem. Rather, we have set out to *improve abundance matching for quenched galaxies*. We introduced a simple new idea that the $\langle \text{SFR} \rangle$ should correlate better with M_{200} for satellites than M_* . We showed empirically that this is the case for a sample of 21 nearby dwarf galaxies (Figure 4). Using this same set of galaxies, we showed further that a power law extrapolation of our abundance matching relation is valid down to $\langle \text{SFR} \rangle \sim 10^{-4} M_{\odot}$, corresponding to $M_{200} \sim 10^9 M_{\odot}$ (Figure 3). We then applied our new $\langle \text{SFR} \rangle - M_{200}$ relation to a volume complete sample of bright Milky Way satellites within 280 kpc to empirically *measure* the cumulative subhalo mass function of the Milky Way. From this, we showed that down to $M_{200} \sim 10^9 M_{\odot}$, the number of observed satellites around the Milky Way sits comfortably within the bounds predicted in ΛCDM (Figure 5, right panel) – i.e. no satellites are ‘missing’. Below this mass limit, ΛCDM predicts many more bound dark matter subhalos should exist. However, our analysis implies that these are not missing, yet. Such subhalos (with masses $M_{200} < 5 \times 10^8 M_{\odot}$) either lie below the detection limit of current surveys (e.g. Koposov et al. 2008, 2015; Bechtol et al. 2015); are completely dark (e.g. Read et al. 2006c); or do not exist at all (which would imply a departure from ΛCDM).

6.4 What about ‘Too Big to Fail’?

Our abundance matching with the $\langle \text{SFR} \rangle$ can be thought of as providing an empirical justification for painting the MW satellites on to the most massive subhalos before infall. Such a mapping has been studied previously in detail and so we know that it produces the correct radial and orbit distribution for the MW classical dSphs (Diemand et al. 2007; Lux et al. 2010), though it may be that the orbits are overly tangential (Lux et al. 2010; Cautun & Frenk 2017). However, a key problem remains. It has long been known that such a mapping predicts central stellar velocity dispersions that are too high to be consistent with the MW classical dSphs (Read et al. 2006b). Boylan-Kolchin et al. (2011) showed that this problem persists for any reasonable mapping between visible dwarfs and DM subhalos, calling it the “Too Big to Fail” (TBTF) problem.

The etymology of TBTF refers to the fact that it can be solved by an *unreasonable* mapping between light and dark. This requires us to leave some of the most massive subhalos before infall devoid of stars, while simultaneously populating lower mass ones. No physical mechanism that could produce such behaviour has been proposed – the more massive

subhalos ought to be “too big to fail” to form stars. However, we have shown here that the MW classical dSphs do indeed appear to inhabit the most massive subhalos before infall, in good agreement with recent analyses that abundance match the satellites directly to simulated subhalos (Jethwa et al. 2018; Kim et al. 2017). In this case, TBTF is really a problem that the central *density* of dwarfs in the Milky Way is lower than expected in pure dark matter ΛCDM structure formation simulations (e.g. Read et al. 2006b; Boylan-Kolchin et al. 2012). This is then identical to the even longer-standing small scale puzzle in ΛCDM : the ‘cusp-core problem’ (Flores & Primack 1994; Moore 1994).

The cusp-core problem refers to the fact that isolated gas rich dwarf irregulars have central dark matter densities that are lower than expected from pure dark matter ΛCDM structure formation simulations. Many solutions to this have been proposed, from modifications to the nature of dark matter (e.g. Spergel & Steinhardt 2000), to bursty star formation physically ‘heating up’ the dark matter, transforming a cusp to a core (e.g. Navarro et al. 1996a; Read & Gilmore 2005; Pontzen & Governato 2012, 2014). Since these solutions act to lower the central densities of dwarf galaxies, they also alleviate the TBTF problem. Indeed, Read et al. (2016a) show that if all of the MW dwarfs had a large dark matter core, we would over-solve TBTF and there would not be enough dense dwarfs to explain the data.

Given the intimate connection between the cusp-core and TBTF problems, we return to both in a separate paper where we measure the internal dark matter densities of a large sample of nearby dIrrs and dSphs (Read et al. 2019).

6.5 Implications for reionisation

Read et al. (2017) found that the smallest star forming dwarf irregulars like Leo T, Aquarius and CVnIdwA likely inhabit dark matter halos with $M_{200} \lesssim 3 \times 10^9 M_{\odot}$ (Figure 3). Assuming the mean mass growth history in ΛCDM , such halos will have a mass $M_{200} \lesssim 6 \times 10^7 M_{\odot}$ at redshift $z = 7$, when reionisation likely completed (e.g. Hazra & Smoot 2017). This mass scale is in tension with many recent cosmological simulations of isolated dwarfs (see the discussion in Read et al. 2017 and Contenta et al. 2017) and with estimates based on the lack of gas rich faint dwarfs in the ALFALFA HI survey (Tollerud & Peek 2017). Here, we also favour a low host-halo mass for Aquarius, CVnIdwA and Carina. However, interestingly, we favour a similarly low halo mass scale for the gas-free galaxies Leo II and Sextans (see Figure 4) and many of the ultra-faint dwarfs (see Figure 5, right panel). The gas-free ultra-faints are substantially more numerous than the classical dwarfs (see the green lines in Figure 5, right panel). This may hint at a solution to the puzzle of the low halo masses of Leo T, Aquarius and CVnIdwA: these galaxies may make up some small fraction of galaxies of mass $M_{200} \sim 1 - 3 \times 10^9 M_{\odot}$, with the rest being ultra-faints that were quenched by reionisation, or some combination of reionisation and ram pressure stripping on infall to the Milky Way (e.g. Gatto et al. 2013). This can occur if this gas-rich subset comprises galaxies that were unusually massive at the epoch of reionisation (e.g. Fitts et al. 2017), or if some process can reignite star formation in a subset of these low mass dwarfs (e.g. Wright et al. 2018). It remains to be seen if such solutions can work in detail.

7 CONCLUSIONS

We have introduced a novel abundance matching technique based on the mean star formation rate $\langle\text{SFR}\rangle$, averaged over the time when a galaxy is forming stars. We compared the masses derived from this relation, M_{200}^{abund} , with direct dynamical estimates for 21 nearby dwarf galaxies, M_{200}^{dyn} , finding excellent agreement between the two (Figure 4). We then used our new $\langle\text{SFR}\rangle$ – M_{200} relation to empirically estimate the cumulative mass function of the Milky Way within 280 kpc of the Galactic centre. Our key results are as follows:

- The cumulative mass function of Milky Way satellites within 280 kpc of the Galactic centre is in good agreement with structure formation simulations in Λ CDM that account for subhalo depletion by the Milky Way disc. We find no evidence for a ‘missing satellites’ problem above $M_{200} \sim 10^9 M_{\odot}$ (Figure 5, right panel).

- Our results imply that the Milky Way ‘classical’ dwarfs inhabit dark matter halos with pre-infall masses in the range $M_{200} \sim 10^9 - 10^{10} M_{\odot}$ (Figure 4), while the ‘ultra-faint’ dwarfs inhabit halos with pre-infall masses in the range $M_{200} \sim 5 \times 10^8 - 5 \times 10^9 M_{\odot}$ (Figure 5, right panel). This provides a new constraint on cosmological hydrodynamical simulations of the Milky Way and its satellites.

- We find that the lowest-mass gas rich dwarf irregulars – Leo T, Aquarius and CVnIrwA – with $M_{200} < 3 \times 10^9 M_{\odot}$ overlap in mass with the Milky Way classical dwarfs (Figure 4). This implies that either the classical dwarfs had their star formation shut down by ram-pressure stripping on infall to the Milky Way (e.g. Gatto et al. 2013), or reionisation has quenched star formation in only a subset of halos at this mass scale.

Our $\langle\text{SFR}\rangle$ – M_{200} abundance matching method can be readily applied to the dwarf satellites of other nearby spiral galaxies like M31 and Centaurus A (e.g. Collins et al. 2013; Crnojević et al. 2016; Carlin et al. 2016; Geha et al. 2017; Müller et al. 2017; Kondapally et al. 2018; Taylor et al. 2018; Mihos et al. 2018; Crnojević et al. 2018; Müller et al. 2018). We will consider this in future work.

8 ACKNOWLEDGMENTS

We would like to thank Jorge Peñarrubia for useful feedback on an early draft of the paper and the anonymous referee for helpful feedback that improved the clarity of this work. JIR would like to thank the KITP in Santa Barbara and the organisers of the ‘‘The Small-Scale Structure of Cold(?) Dark Matter’’ programme. This paper benefited from helpful discussions that were had during that meeting. JIR would like to acknowledge support from STFC consolidated grant ST/M000990/1 and the MERAC foundation. This research was supported in part by the National Science Foundation under Grant No. NSF PHY-1748958.

APPENDIX A: AN ADDITIONAL TEST OF ABUNDANCE MATCHING WITH THE $\langle\text{SFR}\rangle$ – M_{200} RELATION

As an additional test of abundance matching with the the $\langle\text{SFR}\rangle$ – M_{200} relation, in Figure A1 we derive M_{200}^{abund} for

four nearby dwarfs with well-measured star formation histories: Carina, Fornax, WLM and Aquarius. These all have extended star formation that continued up to at least ~ 2 Gyrs ago. In this test, however, we imagine that they fell into the Milky Way t_{trunc} Gyrs ago, causing their star formation to quench. The results of this test are shown in Figure A1 where we show M_{200}^{abund} as a function of t_{trunc} for these galaxies. Notice that Carina, WLM and Aquarius return an estimate of M_{200}^{abund} that is independent of the quenching time, t_{trunc} , within our quoted uncertainties. This occurs because $\langle\text{SFR}\rangle$ for these galaxies is approximately constant. We emphasise that this behaviour is rather different to classical abundance matching using the stellar mass. Imagine, for example, a ‘quenched’ version of WLM that fell into the Milky Way $t_{\text{trunc}} = 5$ Gyrs ago. This ‘quenched’ WLM will have a much lower stellar mass than the real WLM galaxy despite inhabiting a pre-infall dark matter halo of the same mass. In classical abundance matching, this lower stellar mass leads to an inference of M_{200}^{abund} for the ‘quenched’ WLM that is biased low. By contrast, abundance matching with the $\langle\text{SFR}\rangle$ returns an estimate of M_{200}^{abund} that is approximately independent of t_{trunc} .

Finally, notice that Fornax yields a lower M_{200} by a factor ~ 2 if only its old-age stars are used. This could be taken as a measure of the systematic error on M_{200} derived from the $\langle\text{SFR}\rangle$ – M_{200} relation, but a more tantalising possibility is that the rise in the $\langle\text{SFR}\rangle$ at early times for Fornax corresponds to its growth M_{200} prior to infall onto the Milky Way. We will consider this further in future work.

REFERENCES

- Antoja T., et al., 2015, MNRAS, 453, 541
Aparicio A., Carrera R., Martínez-Delgado D., 2001, AJ, 122, 2524
Baldry I. K., Glazebrook K., Driver S. P., 2008, MNRAS, 388, 945
Bate N. F., McMonigal B., Lewis G. F., Irwin M. J., Gonzalez-Solares E., Shanks T., Metcalfe N., 2015, MNRAS, 453, 690
Battaglia G., Sollima A., Nipoti C., 2015, MNRAS, 454, 2401
Bauer A. E., et al., 2013, MNRAS, 434, 209
Bauer J. S., Widrow L. M., Erkal D., 2018, MNRAS, 476, 198
Baugh C. M., 2006, Reports on Progress in Physics, 69, 3101
Bechtol K., et al., 2015, ApJ, 807, 50
Behroozi P. S., Wechsler R. H., Conroy C., 2013, ApJ, 770, 57
Belokurov V., et al., 2007, ApJ, 654, 897
Bermejo-Climent J. R., et al., 2018, preprint, (arXiv:1806.07679)
Blanton M. R., Lupton R. H., Schlegel D. J., Strauss M. A., Brinkmann J., Fukugita M., Loveday J., 2005, ApJ, 631, 208
Boylan-Kolchin M., Bullock J. S., Kaplinghat M., 2011, MNRAS, 415, L40
Boylan-Kolchin M., Bullock J. S., Kaplinghat M., 2012, MNRAS, 422, 1203
Brook C. B., Di Cintio A., Knebe A., Gottlöber S., Hoffman Y., Yepes G., Garrison-Kimmel S., 2014, ApJ, 784, L14
Brown T. M., et al., 2012, ApJ, 753, L21
Bullock J. S., Boylan-Kolchin M., 2017, ARA&A, 55, 343
Carlin J. L., et al., 2016, ApJ, 828, L5
Carrera R., Aparicio A., Martínez-Delgado D., Alonso-García J., 2002, AJ, 123, 3199
Cautun M., Frenk C. S., 2017, MNRAS, 468, L41
Ciucă I., Kawata D., Ando S., Calore F., Read J. I., Mateu C., 2018, MNRAS, 480, 2284

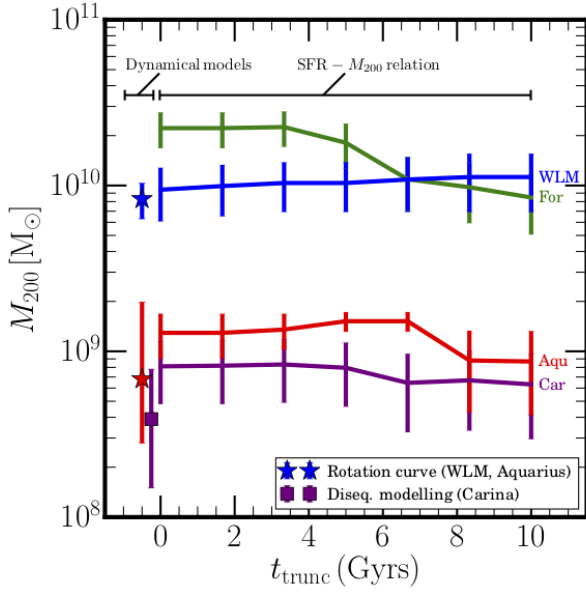


Figure A1. Testing the recovery of the pre-infall M_{200} using our $\langle \text{SFR} \rangle - M_{200}$ abundance matching relation. For this plot, we derive the pre-infall M_{200} for four dwarfs with extended star formation: Carina, Fornax, WLM and Aquarius. We use our $\langle \text{SFR} \rangle - M_{200}$ relation (Figure 3), but artificially truncate the star formation for each dwarf t_{trunc} Gyrs ago. If our abundance matching technique works, then the lines for each dwarf should be flat, recovering the same M_{200} independently of t_{trunc} . This is the case for Carina, WLM and Aquarius within our 68% confidence intervals. Fornax, however, yields a lower M_{200} by a factor ~ 2 if only its old-age stars are used. The stars mark the M_{200} derived from HI rotation curves for WLM and Aquarius (Read et al. 2017). The square marks an independent estimate of the pre-infall M_{200} for Carina from ‘disequilibrium modelling’ (Ural et al. 2015). These are in excellent agreement with the M_{200} derived from the $\langle \text{SFR} \rangle - M_{200}$ relation (see also Figure 4).

Cole A. A., Weisz D. R., Dolphin A. E., Skillman E. D., McConnachie A. W., Brooks A. M., Leaman R., 2014, *ApJ*, 795, 54
 Collins M. L. M., et al., 2013, *ApJ*, 768, 172
 Contenta F., et al., 2017, preprint, ([arXiv:1705.01820](https://arxiv.org/abs/1705.01820))
 Contreras S., Baugh C. M., Norberg P., Padilla N., 2015, *MNRAS*, 452, 1861
 Crnojević D., et al., 2016, *ApJ*, 823, 19
 Crnojević D., et al., 2018, arXiv e-prints,
 D’Onghia E., Springel V., Hernquist L., Keres D., 2010, *ApJ*, 709, 1138
 Davies L. J. M., et al., 2015, *MNRAS*, 447, 1014
 Di Teodoro E. M., Fraternali F., 2015, *MNRAS*, 451, 3021
 Diemand J., Kuhlen M., Madau P., 2007, *ApJ*, 667, 859
 Dolphin A. E., 2000, *ApJ*, 531, 804
 Dolphin A. E., 2002, *MNRAS*, 332, 91
 Drlica-Wagner A., et al., 2015, *ApJ*, 813, 109
 Erkal D., et al., 2018, arXiv e-prints,
 Errani R., Peñarrubia J., Walker M. G., 2018, preprint, ([arXiv:1805.00484](https://arxiv.org/abs/1805.00484))
 Fattahi A., Navarro J. F., Sawala T., Frenk C. S., Sales L. V., Oman K., Schaller M., Wang J., 2016, preprint, ([arXiv:1607.06479](https://arxiv.org/abs/1607.06479))
 Fitts A., et al., 2017, *MNRAS*, 471, 3547
 Flores R. A., Primack J. R., 1994, *ApJ*, 427, L1
 Frenk C. S., White S. D. M., Davis M., Efsthathiou G., 1988, *ApJ*,

327, 507
 Gaia Collaboration et al., 2018, preprint, ([arXiv:1804.09381](https://arxiv.org/abs/1804.09381))
 Garrison-Kimmel S., Bullock J. S., Boylan-Kolchin M., Bardwell E., 2017a, *MNRAS*, 464, 3108
 Garrison-Kimmel S., et al., 2017b, *MNRAS*, 471, 1709
 Gatto A., Fraternali F., Read J. I., Marinacci F., Lux H., Walch S., 2013, *MNRAS*, 433, 2749
 Geha M., Blanton M. R., Yan R., Tinker J. L., 2012, *ApJ*, 757, 85
 Geha M., et al., 2017, *ApJ*, 847, 4
 Gibbons S. L. J., Belokurov V., Evans N. W., 2017, *MNRAS*, 464, 794
 Hazra D. K., Smoot G. F., 2017, preprint, ([arXiv:1708.04913](https://arxiv.org/abs/1708.04913))
 Hearin A. P., Zentner A. R., Berlind A. A., Newman J. A., 2013, *MNRAS*, 433, 659
 Helmi A., White S. D. M., 2001, *MNRAS*, 323, 529
 Hill A. R., Muzzin A., Franx M., Marchesini D., 2017, *ApJ*, 849, L26
 Ibata R. A., Gilmore G., Irwin M. J., 1995, *MNRAS*, 277, 781
 Ibata R. A., Wyse R. F. G., Gilmore G., Irwin M. J., Suntzeff N. B., 1997, *AJ*, 113, 634
 Ibata R., Martin N. F., Irwin M., Chapman S., Ferguson A. M. N., Lewis G. F., McConnachie A. W., 2007, *ApJ*, 671, 1591
 Iorio G., Fraternali F., Nipoti C., Di Teodoro E., Read J. I., Battaglia G., 2017, *MNRAS*, 466, 4159
 Jethwa P., Erkal D., Belokurov V., 2016, *MNRAS*, 461, 2212
 Jethwa P., Erkal D., Belokurov V., 2018, *MNRAS*, 473, 2060
 Katz H., Lelli F., McGaugh S. S., Di Cintio A., Brook C. B., Schombert J. M., 2017, *MNRAS*, 466, 1648
 Kim S. Y., Peter A. H. G., Hargis J. R., 2017, preprint, ([arXiv:1711.06267](https://arxiv.org/abs/1711.06267))
 Klypin A., Kravtsov A. V., Valenzuela O., Prada F., 1999, *ApJ*, 522, 82
 Klypin A. A., Trujillo-Gomez S., Primack J., 2011, *ApJ*, 740, 102
 Kondapally R., Russell G. A., Conselice C. J., Penny S. J., 2018, *MNRAS*, 481, 1759
 Koposov S., et al., 2008, *ApJ*, 686, 279
 Koposov S. E., Belokurov V., Torrealba G., Evans N. W., 2015, *ApJ*, 805, 130
 Kravtsov A. V., Berlind A. A., Wechsler R. H., Klypin A. A., Gottlöber S., Allgood B., Primack J. R., 2004, *ApJ*, 609, 35
 Kravtsov A., Vikhlinin A., Meshcheryakov A., 2014, preprint, ([arXiv:1401.7329](https://arxiv.org/abs/1401.7329))
 Lee M. G., Yuk I.-S., Park H. S., Harris J., Zaritsky D., 2009, *ApJ*, 703, 692
 Lehmann B. V., Mao Y.-Y., Becker M. R., Skillman S. W., Wechsler R. H., 2017, *ApJ*, 834, 37
 Lux H., Read J. I., Lake G., 2010, *MNRAS*, 406, 2312
 Macciò A. V., Kang X., Fontanot F., Somerville R. S., Koposov S., Monaco P., 2010, *MNRAS*, 402, 1995
 Madau P., Diemand J., Kuhlen M., 2008, *ApJ*, 679, 1260
 Mandelbaum R., Seljak U., Kauffmann G., Hirata C. M., Brinkmann J., 2006, *MNRAS*, 368, 715
 Mateo M., Olszewski E. W., Walker M. G., 2008, *ApJ*, 675, 201
 Mayer L., Governato F., Kaufmann T., 2008, *Advanced Science Letters*, 1, 7
 McConnachie A. W., 2012, *AJ*, 144, 4
 Mihos J. C., Durrell P. R., Feldmeier J. J., Harding P., Watkins A. E., 2018, *ApJ*, 862, 99
 Mitchell P. D., Lacey C. G., Baugh C. M., Cole S., 2013, *MNRAS*, 435, 87
 Miyamoto M., Nagai R., 1975, *PASJ*, 27, 533
 Mobasher B., et al., 2015, *ApJ*, 808, 101
 Moore B., 1994, *Nature*, 370, 629
 Moore B., Ghigna S., Governato F., Lake G., Quinn T., Stadel J., Tozzi P., 1999, *ApJ*, 524, L19
 Moster B. P., Somerville R. S., Maulbetsch C., van den Bosch F. C., Macciò A. V., Naab T., Oser L., 2010, *ApJ*, 710, 903

- Müller O., Scalera R., Binggeli B., Jerjen H., 2017, *A&A*, 602, A119
- Müller O., Jerjen H., Binggeli B., 2018, *A&A*, 615, A105
- Navarro J. F., Eke V. R., Frenk C. S., 1996a, *MNRAS*, 283, L72
- Navarro J. F., Frenk C. S., White S. D. M., 1996b, *ApJ*, 462, 563
- Niederste-Ostholt M., Belokurov V., Evans N. W., Peñarrubia J., 2010, *ApJ*, 712, 516
- Niederste-Ostholt M., Belokurov V., Evans N. W., 2012, *MNRAS*, 422, 207
- Oh S.-H., et al., 2015, *AJ*, 149, 180
- Peñarrubia J., Gómez F. A., Besla G., Erkal D., Ma Y.-Z., 2016, *MNRAS*, 456, L54
- Peacock J. A., 1999, *Cosmological physics. Cosmological physics.* Publisher: Cambridge, UK: Cambridge University Press, 1999. ISBN: 0521422701
- Peacock J. A., Smith R. E., 2000, *MNRAS*, 318, 1144
- Peng Y.-j., et al., 2010, *ApJ*, 721, 193
- Peng Y.-j., Lilly S. J., Renzini A., Carollo M., 2012, *ApJ*, 757, 4
- Percival W. J., 2013, preprint, ([arXiv:1312.5490](https://arxiv.org/abs/1312.5490))
- Pontzen A., Governato F., 2012, *MNRAS*, 421, 3464
- Pontzen A., Governato F., 2014, *Nature*, 506, 171
- Power C., Navarro J. F., Jenkins A., Frenk C. S., White S. D. M., Springel V., Stadel J., Quinn T., 2003, *MNRAS*, 338, 14
- Read J. I., Gilmore G., 2005, *MNRAS*, 356, 107
- Read J. I., Steger P., 2017, *MNRAS*, 471, 4541
- Read J. I., Wilkinson M. I., Evans N. W., Gilmore G., Kleyna J. T., 2006a, *MNRAS*, 366, 429
- Read J. I., Wilkinson M. I., Evans N. W., Gilmore G., Kleyna J. T., 2006b, *MNRAS*, 367, 387
- Read J. I., Pontzen A. P., Viel M., 2006c, *MNRAS*, 371, 885
- Read J. I., Agertz O., Collins M. L. M., 2016a, *MNRAS*, 459, 2573
- Read J. I., Iorio G., Agertz O., Fraternali F., 2016b, *MNRAS*, 462, 3628
- Read J. I., Iorio G., Agertz O., Fraternali F., 2017, *MNRAS*, 467, 2019
- Read J. I., Walker M. G., Steger P., 2018, *MNRAS*, 481, 860
- Read J. I., Walker M. G., Steger P., 2019, *MNRAS*, 484, 1401
- Reddick R. M., Wechsler R. H., Tinker J. L., Behroozi P. S., 2013, *ApJ*, 771, 30
- Reed D. S., Bower R., Frenk C. S., Jenkins A., Theuns T., 2007, *MNRAS*, 374, 2
- Ruiz-Lara T., et al., 2015, *A&A*, 583, A60
- Sawala T., et al., 2016, *MNRAS*, 457, 1931
- Sawala T., Pihajoki P., Johansson P. H., Frenk C. S., Navarro J. F., Oman K. A., White S. D. M., 2017, *MNRAS*, 467, 4383
- Scannapieco C., et al., 2012, *MNRAS*, 423, 1726
- Spencer M. E., Mateo M., Walker M. G., Olszewski E. W., 2017, *ApJ*, 836, 202
- Spergel D. N., Steinhardt P. J., 2000, *Physical Review Letters*, 84, 3760
- Springel V., 2005, *MNRAS*, 364, 1105
- Springel V., Frenk C. S., White S. D. M., 2006, *Nature*, 440, 1137
- Springel V., et al., 2008, *MNRAS*, 391, 1685
- Taylor M. A., Eigenthaler P., Puzia T. H., Muñoz R. P., Ribbeck K. X., Zhang H.-X., Ordenes-Briceño Y., Bovill M. S., 2018, *ApJ*, 867, L15
- Tollerud E. J., Peek J. E. G., 2017, preprint, ([arXiv:1711.00485](https://arxiv.org/abs/1711.00485))
- Tollerud E. J., Bullock J. S., Strigari L. E., Willman B., 2008, *ApJ*, 688, 277
- Tomozeiu M., Mayer L., Quinn T., 2016, *ApJ*, 827, L15
- Ural U., Wilkinson M. I., Read J. I., Walker M. G., 2015, *Nature Communications*, 6, 7599
- Vale A., Ostriker J. P., 2004, *MNRAS*, 353, 189
- Vale A., Ostriker J. P., 2006, *MNRAS*, 371, 1173
- Walcher J., Groves B., Budavári T., Dale D., 2011, *Ap&SS*, 331, 1
- Walker M. G., Mateo M., Olszewski E. W., 2009a, *AJ*, 137, 3100
- Walker M. G., Mateo M., Olszewski E. W., Peñarrubia J., Wyn Evans N., Gilmore G., 2009b, *ApJ*, 704, 1274
- Walker M. G., Olszewski E. W., Mateo M., 2015, *MNRAS*, 448, 2717
- Weisz D. R., Dolphin A. E., Skillman E. D., Holtzman J., Gilbert K. M., Dalcanton J. J., Williams B. F., 2014, *ApJ*, 789, 147
- Wetzel A. R., Hopkins P. F., Kim J.-h., Faucher-Giguère C.-A., Kereš D., Quataert E., 2016, *ApJ*, 827, L23
- White S. D. M., Rees M. J., 1978, *MNRAS*, 183, 341
- Wright A. H., et al., 2017, *MNRAS*, 470, 283
- Wright A. C., Brooks A. M., Weisz D. R., Christensen C. R., 2018, preprint, ([arXiv:1802.03019](https://arxiv.org/abs/1802.03019))
- Wuyts S., Franx M., Cox T. J., Hernquist L., Hopkins P. F., Robertson B. E., van Dokkum P. G., 2009, *ApJ*, 696, 348
- Zentner A. R., Berlind A. A., Bullock J. S., Kravtsov A. V., Wechsler R. H., 2005, *ApJ*, 624, 505
- Zhang H.-X., Hunter D. A., Elmegreen B. G., Gao Y., Schrupa A., 2012, *AJ*, 143, 47
- Zolotov A., et al., 2012, *ApJ*, 761, 71
- de Boer T. J. L., et al., 2012a, *A&A*, 539, A103
- de Boer T. J. L., et al., 2012b, *A&A*, 544, A73
- de Boer T. J. L., Tolstoy E., Lemasle B., Saha A., Olszewski E. W., Mateo M., Irwin M. J., Battaglia G., 2014, *A&A*, 572, A10
- de Boer T. J. L., Belokurov V., Koposov S., 2015, *MNRAS*, 451, 3489
- van der Marel R. P., 2006, in *The Local Group as an Astrophysical Laboratory*. pp 47–71 ([arXiv:astro-ph/0404192](https://arxiv.org/abs/astro-ph/0404192))